DRAFT VERSION OCTOBER 22, 2015
Preprint typeset using LaTeX style emulateapj v. 12/16/11

AN INTERMEDIATE-BAND SURVEY FOR STRONG LINE EMITTERS IN THE COSMOS 2 SQUARE DEGREE FIELD*: I. HIGH REDSHIFT LYMAN α EMITTERS

MASAKAZU A. R. KOBAYASHI[1], YOSHIAKI TANIGUCHI[1], MASARU KAJISAWA[1,2], TOHRU NAGAO[1], YASUHIRO SHIOYA1[1], NICK Z. SCOVILLE[3], DAVID B. SANDERS[4], PETER L. CAPAK[3,5], ANTON M. KOEKEMOER[6], HENRY J. MCCRACKEN[7], OLIVIER LE FÈVRE[8], LIDIA TASCA[8], KARTIK SHETH[9], ALVIO RENZINI[10], SIMON LILLY[11], MARCELLA CAROLLO[11], KATARINA KOVAČ[11], OLIVIER ILBERT[8], AND EVA SCHINNERER[12],

Draft version October 22, 2015

ABSTRACT

We have carried out an intermediate-band optical survey for high redshift strong Lyman α Emitters (hereafter LAEs) in the COSMOS 2 Square Degree Field using the Suprime-Cam on the Subaru Telescope. The use of 12 intermediate-band optical filters with a spectroscopic resolution of $\lambda/\Delta\lambda = 23$ enables us to discover a large sample of 527 LAEs at $z = 2.5$–5.8 with large rest-frame equivalent widths of Lyα emission, $EW_0 >$ xx Å. Since our new LAEs are systematically stronger ones, they have been missed in previous LAE surveys. First, we discuss their observational properties such as star formation rate (SFR), stellar mass, dust extinction, luminosity function, and space density as a function of redshift. Second, we compare these properties with those of LAEs previously studied. Then, we have found the following new results.

.....

.....

.....

Based on these new results, we discuss early star formation history in galaxies at high redshift.

Keywords: cosmology: observations — cosmology: early universe — galaxies: formation — galaxies: evolution — galaxies: high-redshift

1. INTRODUCTION

Searching for high-redshift galaxies is essentially important in the whole understanding of the formation and early evolution of galaxies. The appearance of 8–10 m class telescopes have been contributing to the progress in this research field and there are now a large samples of high-redshift galaxies beyond redshift of $z \sim 2$–3, the peak era of the cosmic star formation in early universe (refs). Indeed, by using the Lyman break method, probable candidates of galaxies beyond $z \sim 10$ have been found in the Hubble Ultra Deep Field and the Hubble Frontier Field (refs). On one hand, deep imaging surveys with optical narrowband filters are also successful in the discovery of many young galaxies up to $z \sim 7$ (refs). In addition, the so-called dark side of galaxy evolution has also been probed by infrared and radio deep surveys to date (refs). These studies together with surveys of low- and intermediate-redshift galaxies have revealed the cosmic star-formation history as well as star formation properties of galaxies as a function of redshift. However, the question arises as whether we have already probed all types of high-redshift populations or not. This is attributed to the general difficulty in finding rare populations at high redshift because of both limited survey areas and depths.

What types of galaxies have been missed in previous surveys? One population is dwarf galaxies. Although they are numerous even at high redshift, they are too faint to be detected den if we use 8–10 m class telescopes. Another important population is most massive galaxies. Being the so-called down-sizing evolution of galaxies taken into account (Cowie et al. 1996), it is important to explore the nature of such most massive galaxies at high redshift. In order to find these two populations at high redshift, we have conducted our unique optical deep and wide imaging survey using 12 intermediate-band filters with the Suprime-Cam on the Subaru Telescope. The spectroscopic resolution of these filters is $\lambda/\Delta\lambda = 23$. Therefore, we are able to find very strong Lyα emitters (LAEs) even though they are too faint in their continuum magnitude. Another merit of our survey is that our survey field is the HST COSMOS field. This wide-field survey is expected to detect rare populations such as most massive LAEs although their volume density could be low.

kobayashi@cosmos.phys.sci.ehime-u.ac.jp

* Based on observations with NASA/ESA *Hubble Space Telescope*, obtained at the Space Telescope Science Institute, which is operated by AURA, Inc., under NASA contract NAS 5-26555; and also based on data collected at Subaru Telescope, which is operated by the National Astronomical Observatory of Japan; and also based on data products from observations made with ESO Telescopes at the La Silla Paranal Observatory under ESO programme ID 179.A-2005 and on data products produced by TERAPIX and the Cambridge Astronomy Survey Unit on behalf of the UltraVISTA consortium.

[1] Research Center for Space and Cosmic Evolution, Ehime University, Bunkyo-cho, Matsuyama 790-8577, Japan

[2] Graduate School of Science and Engineering, Ehime University, Bunkyo-cho, Matsuyama 790-8577, Japan

[3] Department of Astronomy, MS 105-24, California Institute of Technology, Pasadena, CA 91125, USA

[4] Institute for Astronomy, University of Hawaii, 2680 Woodlawn Drive, Honolulu, HI 96822, USA

[5] Spitzer Science Center, California Institute of Technology, Pasadena, CA 91125, USA

[6] Space Telescope Science Institute, 3700 San Martin Drive, Baltimore, MD 21218, USA

[7] Institut d'Astrophysique de Paris, UMR7095 CNRS, Université Pierre et Marie Curie, 98 bis Boulevard Arago, 75014, Paris, France

[8] Aix Marseille Université, CNRS, LAM (Laboratoire d'Astrophysique de Marseille), UMR 7326, 13388, Marseille, France

[9] National Radio Astronomy Observatory, 520 Edgemont Road, Charlottesville, VA 22903, USA

[10] Dipartimento di Astronomia, Universita di Padova, vicolo dell'Osservatorio 2, 35122, Padua, Italy

[11] Department of Physics, ETH Zurich, 8093, Zurich, Switzerland

[12] MPI for Astronomy, Königstuhl 17, D-69117 Heidelberg, Germany

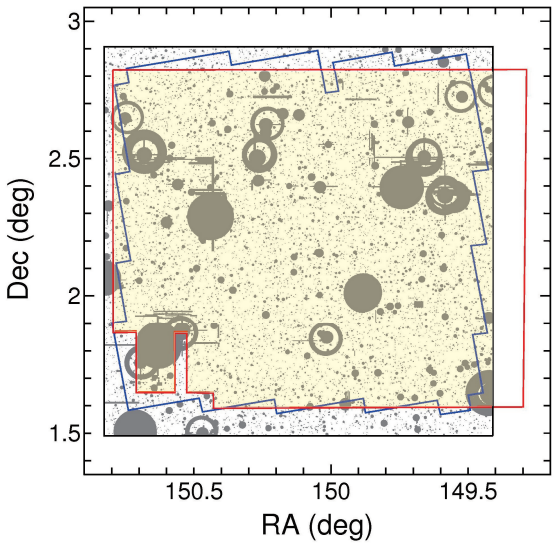

Figure 1. The COSMOS deep area, the UltraVISTA area, and the HST/ACS area are shown by black, red, and blue lines, respectively. Our survey area is the overlapped region between the COSMOS deep and UltraVISTA areas shown by shaded yellow color. The masked-out areas are shown by gray color.

2. DATA AND SAMPLE SELECTION

2.1. *Data*

The photometric catalog used in our analysis is the latest version of the COSMOS official photometric catalog (version Feb. 2012) prepared by Peter Capak together with the photometric zero-point offsets given in the COSMOS photometric redshift catalog (version 2) prepared by Olivier Ilbert (see for the derivation of offsets, Ilbert et al. 2009). Note that the combined i' and i^* image was used as the detection image of the official photometric catalog (Capak et al. 2007). Our sample selection is therefore based on the i-band selected catalog. Note also that UltraVISTA DR1 data (McCracken et al. 2012) are also included.

The survey area is the overlapped region between the COSMOS 2 square degree field for which homogeneous and deepest data are available (flag = 0 in the DEEP mask) and the UltraVISTA areas. We do not use the masked areas in B, V, i', or z' band given in the COSMOS official photometric catalog. We also do not use the masked-out areas in the 12 IA bands defined by us. Then, the final survey area covers a field of 1.34 deg^2 as shown in Figure 1.

2.2. *Sample Selection*

We select strong LAEs from all objects detected in our survey area of 1.34 deg^2 through the following four steps: (1) selection of IA-band excess objects, (2) line identification and photometric redshift ($z_{\rm ph}$) estimate, (3) real emitter selection using best-fit model SED, and (4) rejection of possible AGN. In the following sections, we describe the details in each step. Note that, although these procedures are applicable for all types of strong line emitters in our survey, we describe our method to identify only strong LAEs here for simplicity. The flowcharts for these procedures are given in Appendix B.

2.2.1. *Step 1: Selection of IA-band Excess Objects*

As the first step, we have selected IA-band excess objects using the following two criteria:

$$IA_{\rm c} - IA \geq 0.3, \tag{1}$$

and

$$IA_{\rm c} - IA \geq 3\sigma_{\rm IA_c-IA}, \tag{2}$$

where $IA_{\rm c}$ is the magnitude of the frequency-matched continuum for a concerned IA filter band, that is estimated by using two adjacent broadband magnitudes as described in detail below. The 3σ error of $IA_{\rm c} - IA$, $3\sigma_{\rm IA_c-IA}$, is evaluated by using

$$3\sigma_{\rm IA_c-IA} = -2.5\log\left(1 - 3\sqrt{\sigma_{\rm IAc}^2 + \sigma_{\rm IA}^2}\Big/ f_{\rm IA}\right), \tag{3}$$

where $\sigma_{\rm IAc}$ and $\sigma_{\rm IA}$ are the 1-σ flux errors for the frequency-matched continuum and IA band, respectively, given in Table 1 and $f_{\rm IA}$ is the flux in the IA band.

In our analysis of this step 1, we do not use any broadband photometry that overlaps a concerned IA filter bandpass because the strong emission may affect the broadband photometry (e.g., Cardamone et al. 2009; Taniguchi et al. 2010; Huang et al. 2015 and references therein). Then, we estimate the frequency-matched continuum flux, $f_{\rm c,IA_{\it i}}$, for each IA-band IA$_i$ via the following linear combination:

$$f_{\rm c,IA_{\it i}} = a_i f_{\rm BB_{\it i,1}} + (1-a_i) f_{\rm BB_{\it i,2}}, \tag{4}$$

where $f_{\rm BB_{\it i,1}}$ and $f_{\rm BB_{\it i,2}}$ are the flux densities of the BB$_{i,1}$- and BB$_{i,2}$-bands, respectively, which are adjacent to but do not overlap the bandpass of the IA-band IA$_i$. The coefficient of a_i in Equation (4) is determined via the following condition: $a_i = (\nu_i - \nu_{\rm BB_{\it i,2}})/(\nu_{\rm BB_{\it i,1}} - \nu_{\rm BB_{\it i,2}})$, where ν_i, $\nu_{\rm BB_{\it i,1}}$, and $\nu_{\rm BB_{\it i,2}}$ are the effective frequencies of the IA$_i$-, BB$_{i,1}$-, and BB$_{i,2}$-bands, respectively. The combination of broadband filters of BB$_{i,1}$ and BB$_{i,2}$ and the coefficient of a_i for each IA-band are compiled in Table 1. The first criterion represented by Equation (1) roughly correspond to $EW_{\rm obs} \gtrsim 150$ Å. These two criteria of Equations (1) and (2) are shown in Figure 2.

In this step 1, we have selected IA-excess objects that satisfy both the criteria of Equation (1) and (2). The diagram of IA-excess vs. IA magnitude is shown in Figure 2 for each IA filter band. In this way, we have selected a sample of 5357 IA-excess objects. Note that some objects show IA-excess emission in more than one filter, resulting 5957 IA-excess features in total, as shown in Table 2.

2.2.2. *Step 2: Identification of Emission Lines*

In order to identify which emission line contributes to the observed IA-excess feature, we carry out spectral energy distribution (SED) fitting. This procedure is our step 2.

Since our IA filters cover a wavelength range from 427 nm to 827 nm, it is expected that the following rest-frame ultraviolet and optical emission lines are main contributors to IA-excess feature: Lyα, C IV, C III], Mg II, [O II], [O III] + Hβ, and Hα + [N II]. Usually, we observe the excess emission in a single filter band. In some cases, however, we may observe the excess emission in more than one filter band. We have simulated such multiband excess phenomena and found that the maximum number of excess filter bands is four. However, it is found that 24 objects show more than four excess filter bands, as presented in Table 2[14]. One probable interpretation is that these 24 objects are variable sources such as blazers; i.e., their IA band magnitudes are affected by such time variations. Our broadband data were obtained during a period between 2004 January and 2005 April. On the other hand, our

[14] The sum of the total number of the excess objects for $N_{\rm ex}^{\rm temp} > 4$ provides 24.

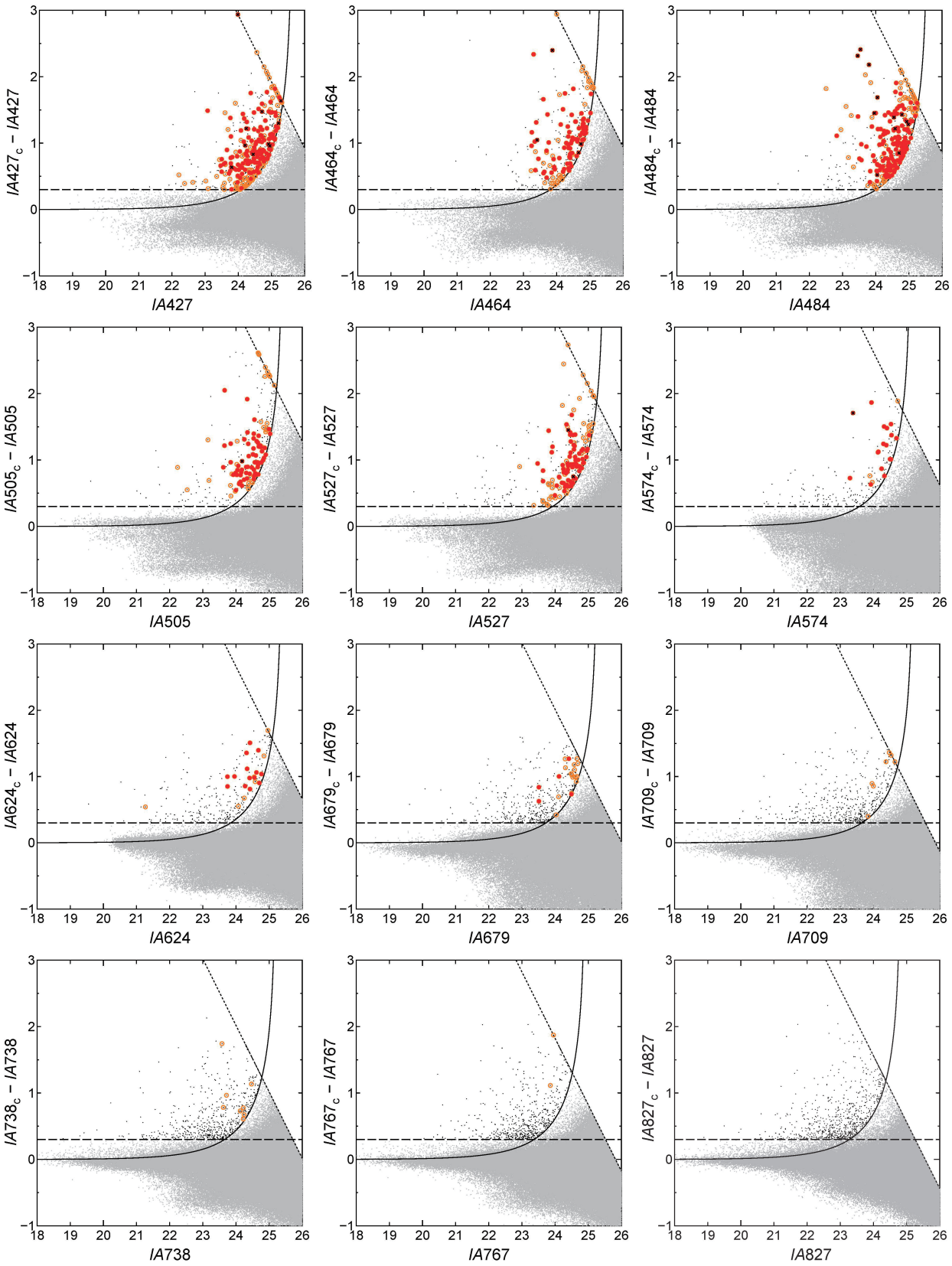

Figure 2. Color-magnitude diagrams of 12 IA-bands for all sources detected in each IA-band in the COSMOS field. In each panel, the horizontal dashed line corresponds to the first criterion represented by Equation (1) and the solid curve shows the second criterion represented by Equation (2). The dotted line represents the 3σ limiting magnitude of IA_c; all sources fainter than 3σ limiting magnitude in IA_c are placed at the 3σ limiting magnitude. The orange-open and red-filled circles are the 865 and 527 LAEs selected by step 2 and step 3, respectively. For the possible AGNs identified in step 4, black crosses are overlayed on the red-filled circles. **The 63 LAEs with $EW_0 \geq 100$ Å are shown by blue-filled circles.**

Table 1
Quantities Related to the Step 1 of Our Sample Selection

IA_i	$BB_{i,1}$	$BB_{i,2}$	Effective frequencies (THz)[a]			a_i	3σ limiting magnitudes[b]	
			ν_i	$\nu_{BB_{i,1}}$	$\nu_{BB_{i,2}}$		IA	IA_c
IA427	u^*	V	704.35	766.54	550.19	0.7126	25.8	26.8–27.8
IA464	u^*	V	647.04	766.54	550.19	0.4477	25.6	26.9–27.2
IA484	u^*	V	618.65	766.54	550.19	0.3164	25.9	26.8–26.9
IA505	B	r'	592.39	675.27	481.07	0.5732	25.6	27.3
IA527	B	r'	570.07	675.27	481.07	0.4583	25.7	27.1
IA574[c]	g'	i'	520.28	634.04	392.96	0.5281	25.4	26.6
		i^*			392.97	0.5281		24.9
IA624[c]	V	i'	481.21	550.19	392.96	0.5613	25.7	26.7
		i^*			392.97	0.5612		24.9
IA679	V	z'	442.25	550.19	332.31	0.5046	25.3	26.0
IA709	V	z'	423.99	550.19	332.31	0.4208	25.4	25.9
IA738	r'	z'	407.40	481.07	332.31	0.5048	25.4	26.0
IA767	r'	z'	390.29	481.07	332.31	0.3898	25.1	25.8
IA827	r'	z'	363.79	481.07	332.31	0.2116	25.1	25.6

[a] The effective frequencies for these filters are calculated from their effective wavelengths given in Table 1 of Ilbert et al. (2009).
[b] The limiting magnitude defined by a 3σ sky noise in a $3''$ diameter circular aperture except for the limiting magnitudes of the IAc for IA427, IA464, and IA484. They are defined separately for each object since the 3σ limiting magnitude of the u^* band significantly depends on the place in the COSMOS field.
[c] To evaluate the frequency-matchced continuum of both IA574 and IA624-band filters, the CFHT i^*-band magnitude is used for the objects which saturate in the Subaru i'-band image; otherwise, the Subaru i'-band magnitude is used. Note that, while the effective frequencies of the Subaru i' and CFHT i^* bands are similar with each other, the 3σ limiting magnitudes are significantly different: 26.1 mag and 24.0 mag for the Subaru i' and CFHT i^* bands, respectively.

Table 2
Number of the IA-band Excess Candidates in Step 1.

IA-band	$N_{>3\sigma}$[a]	Number $N(N_{ex}^{temp})$[b]												
		$N(1)$	$N(2)$	$N(3)$	$N(4)$	$N(5)$	$N(6)$	$N(7)$	$N(8)$	$N(9)$	$N(10)$	$N(11)$	$N(12)$	Total
IA427	144,978	517	26	10	2	3	1	1	2	1	3	0	1	567
IA464	133,658	401	45	14	6	4	2	1	3	0	2	0	1	479
IA484	201,252	692	56	10	8	4	2	1	4	1	1	0	1	780
IA505	157,983	338	29	13	5	6	2	2	4	1	3	0	1	404
IA527	182,770	364	65	14	8	5	1	1	4	1	3	0	1	467
IA574	145,063	240	47	9	6	3	1	0	2	0	3	0	1	312
IA624	231,075	399	74	16	9	3	1	1	4	1	2	0	1	511
IA679	213,234	457	35	19	5	2	2	2	5	1	3	0	1	532
IA709	211,537	425	74	17	3	4	2	0	3	1	3	0	1	533
IA738	222,216	528	112	10	4	4	2	2	4	1	2	0	1	670
IA767	178,159	523	85	3	2	2	1	1	3	1	2	0	1	624
IA827	197,909	832	70	15	2	5	1	2	2	0	3	0	1	933
Total (excess IA-band)[c]	2,219,834	5716	718	150	60	45	18	14	40	9	30	0	12	6812
Total (excess object)[d]	299,090	5716	359	50	15	9	3	2	5	1	3	0	1	6164

[a] The total number of the objects brighter than the 3σ limiting magnitude in the IA band, which is shown in Table 1.
[b] N_{ex}^{temp} is the integer variable which represents the number of the IA bands satisfying both of the selection criteria of Equations (1) and (2) (see Figure A1).
[c] The total number of the excess IA-bands in the IA-band detected objects; it is simply calculated as the sum of $N(N_{ex}^{temp})$ for all IA-band filters.
[d] The total number of the sample IA-excess candidates, which is not overlapped at all; it is counted as the sum of $N(N_{ex}^{temp})/N_{ex}^{temp}$ for all IA-band filters.

IA filter observations were made in the two epochs: i) from 2006 January to 2006 February (i.e., IA427, IA464, IA505, IA574, IA679, IA709, and IA827) and ii) from 2006 December to 2007 March (i.e., IA484, IA527, IA624, IA738, and IA767). In order to remove such variable objects, we have adopted the following criterion; objects with the median of $IA_c - IA > 0.3$ in either of the IA observing epochs are variable sources (see Salvato et al. 2009). Since we have found that all the 24 objects are identified as variable sources, we do not use them in our further analysis. Then, we have a sample of 5333 objects.

For these 5333 objects, we apply the photometric redshift estimate code EAZY (Brammer et al. 2008) and estimate both the reduced χ-square, $\chi^2_\nu(z)$, and the volume-weighted likelihood, $p(z)$ [$= (dV(z)/dz)e^{-\chi^2_\nu(z)/2}$, where $V(z)$ is the comoving volume which corresponds to the survey area], to identify the emission line causing the observed IA excess. In this analysis, we use the following 27 filter data; CFHT (u^*, i^*), Subaru ($BgVr'i'z'$, z''[15], 12 IAs), UltraVISTA ($YJHK$), and IRAC (ch1, ch2). Note, however, that we do not use any broadband data overlapped with a concerned IA excess bandpass as well as the excess IA band itself. Since the photometric error for brighter objects is underestimated in the SExtractor output, we adopt 0.03 mag[16] for such objects. On the other hand, when only 3σ upper limit data are available, we set the flux density to be $f_\nu = 1.5\sigma \pm 1\sigma$ in our photometric redshift estimate.

In the line identification procedure, we adopt the following acceptable condition; $\chi^2_\nu(z)$ must be ≤ 3 for a case that a strong emission line is expected to be observed in an IA filter band at a reasonable redshift range. Note, however, that two or more emission lines are acceptable due to the behavior of $\chi^2_\nu(z)$. On the other hand, no emission line is acceptable for some sources; in this case, we consider that their IA-band excess is not attributed to a strong emission line (e.g., misidentification by a Balmer break, and so on).

For objects with a single IA excess band, we identify their emission line as that with the highest probability in the volume-weighted likelihood $p(z)$ among possible emission lines. For objects with more than single IA excess band, we identify their combination of emission lines as that with the highest $p(z)$ among possible emission lines. For objects with two adjacent IA excess filter bands (e.g, IA464 and IA484), we adopt their redshifts calculated from the central wavelengths of the overlapped bandpasses of the two filter bands. In this way, we have obtained a sample of 865 LAE candidates. Note that the total number of IA excess bands due to Lyα emission is 885, as shown in Table 3.

- Figure xx: χ_ν vs. z **<– is this required? if yes, how is this figure shown? for only some sources??**

2.2.3. *Step 3: Selection of Real LAEs*

Finally, we select a sample of LAEs via a SED fitting using SED templates generated with GALAXEV (Bruzual & Charlot 2003). The adopted parameters are summarized in Table 4.

Since LAEs tend to be faint in the continuum, only upper limit data may be available in IA-band data. In this case, it is usually difficult to obtain a reliable SED fitting result. Therefore, before SED fitting is executed, we remove LAE candidates with upper limit data in more than or equal to six IA filter bands; 150 objects are removed by this criterion. Then, we obtain a sample of 715 LAE candidates.

In the SED fitting, the redshift of the LAE candidates is fixed at $z_{\rm ph}$ determined via step 2. We use the following 29 photometric data: CFHT (u^* and i^*), Subaru ($BgVr'i'z'$, z'', and 12 IA bands), UltraVISTA ($YJHK$), and Spitzer IRAC (ch1–4). Here, we use newly both ch3 and ch4 photometry of IRAC data in order both to obtain more accurate physical properties and to remove objects dominated by AGN component. Note that we do not use both any broadband data overlapped with a concerned IA-excess band as well as the excess IA band itself and any optical filter bands in which a strong emission line is expected. We also do not use both broadband and IA bands shorter than the Lyman limit. However, we use all JHK-band data even if some strong rest-frame optical emission lines are expected. The reason for this prescription is that the effect of such emission lines is not expected to be serious because of their broader filter bandpasses. Using the results of the SED fitting, we remove the LAE candidates having the best-fit SED at $z = z_{\rm ph}$ with $\chi^2_\nu(z_{\rm ph}) > 3$; 74 objects are removed and 641 LAE candidates are obtained.

Then, in order to verify the strong excess emission in an IA band, we also adopt another criterion of $EW_0 > EW_{{\rm err},3\sigma}$, where $EW_{{\rm err},3\sigma}$ is the estimated error in EW within a range of $\Delta\chi^2 \leq 6.63$. In this calculation, we use the mean continuum flux density of the best-fit SED model between the rest-frame 1300 Å and 1400 Å to obtain both of EW_0 and $EW_{{\rm err},3\sigma}$ since the continuum flux density shorter than the Lyα emission is strongly absorbed by intergalactic medium. In this way, 84 objects are rejected and a sample of 557 LAE candidates are obtained as shown in Table 5. Note that, as a single LAE candidate have two adjacent excess IA-bands (i.e., IA484 and IA505[17]), the total number of the excess IA-band is 570.

2.2.4. *Step 4: Rejection of Possibly AGN-powered LAEs*

As the final procedure to select LAEs, we remove the candidates of AGNs from our LAE sample because our main interest is to investigate the star-formation activity in galaxies at high redshift. For this purpose, we adopt the following three criteria. (1) The IRAC color criteria proposed by Donley et al. (2012), which are shown in Figure 3; using these criteria, we can remove a sample of sources with power-law like rest-frame near infrared continuum. As a result, 25 sources are removed. (2) X-ray sources; we have removed 3 X-ray sources detected within an error circle by XMM-Newton using the XMM-COSMOS database (Hasinger et al. 2007). And (3) radio sources; we have removed 3 radio sources detected by VLA within a radius of 1 arcsec using the VLA-COSMOS database (Schinnerer et al. 2007).

While the simple sum of the possible AGNs from the above three criteria is 31, one of the X-ray sources also satisfies the IRAC color criteria. Therefore, 30 objects are rejected from our LAE sample as possible AGNs in total. As a result, we obtain our final sample of 527 LAEs at $z_{\rm ph} = 2.5$–4.6. Since

[15] The z'' is z' band data taken with the new red-sensitive CCD chips on the Subaru/Suprime-Cam (Furusawa et al. 2015, private communication). We use both of z''- and z'-band images if z''-band image is available, while z''-band images are available only for a part of our survey field **(xxx%)**.

[16] The photometric error is estimated as 0.01 mag in Ilbert et al. (2009). However, taking account of the uncertainty in the zero point correction, we adopt 0.03 mag in our analysis.

[17] We assume that the excesses in the two adjacent IA-bands are caused by a single Lyα emission line at the central wavelength of the overlapped bandpasses of IA484 and IA505. Hence, the photometric redshift of the LAE candidate is adopted to be **xxx**.

Table 3
Number of LAE Candidates in Step 2.

IA-band	$z_{\rm ph}$[a]	$z_{\rm min}$–$z_{\rm max}$[b]	Number $N(N_{\rm ex}^{\rm cons})$		
			$N(1)$	$N(2)$	Total
IA427	2.501	2.416–2.586	244	1	245
IA464	2.811	2.722–2.901	149	4	153
IA484	2.986	2.892–3.080	310	8	318
IA505	3.163	3.068–3.258	100	15	115
IA527	3.326	3.226–3.425	136	13	149
IA574	3.740	3.628–3.851	24	0	24
IA624	4.125	4.001–4.248	35	0	35
IA679	4.576	4.438–4.714	18	1	19
IA709	4.816	4.686–4.946	4	2	6
IA738	5.053	4.920–5.186	7	1	8
IA767	5.318	5.169–5.468	2	0	2
IA827	5.779	5.637–5.920	0	0	0
Total (excess IA-band)	...	...	1029	45	1074
Total (excess object)	...	...	1029	26[c]	1055

[a] Photometric redshift determined based on the assumption that Lyα emission is located at the effective wavelength of the bandpass of each IA band for the LAE candidates with $N_{\rm ex}^{\rm cons} = 1$. For the LAE candidates with $N_{\rm ex}^{\rm cons} > 1$, $z_{\rm ph}$ can be different from $z_{\rm ph}$ for those with $N_{\rm ex}^{\rm cons} = 1$ since it is determined from the redshift range in which $N_{\rm ex}^{\rm cons}$ emission lines enter simultaneously in $N_{\rm ex}^{\rm cons}$ excess bands.
[b] Redshift range probed by each IA-band filter for Lyα emission calculated from its effective wavelength and full width at the half maximum.
[c] 19 LAE candidates have two adjacent excess IA-bands, which are considered to be caused by a single Lyα line. The combinations of the two excess IA-bands for these LAE candidates are the following: (IA464, IA484) for 3 LAE candidates at $z_{\rm ph} = 2.896$, (IA484, IA505) for 3 LAE candidates at $z_{\rm ph} = 3.073$, (IA505, IA527) for 11 LAE candidates at $z_{\rm ph} = 3.241$, (IA679, IA709) for 1 LAE candidate at $z_{\rm ph} = 4.699$, and (IA709, IA738) for 1 LAE candidate at $z_{\rm ph} = 4.931$. The other 7 LAE candidates have two separated excess IA-bands, which are considered to be caused by Lyα and C IV or Lyα and C III]. The combinations of two excess IA-bands for these LAE with C IV or LAE with C III] candidates are the following: (IA427, IA527) for 1 LAE with C IV candidate at $z_{\rm ph} = 2.444$, (IA464, IA574) for 1 LAE with C IV candidate at $z_{\rm ph} = 2.764$, (IA464, IA709) for 1 LAE with C III] candidate at $z_{\rm ph} = 2.754$, (IA464, IA738) for 1 LAE with C III] candidate at $z_{\rm ph} = 2.835$, (IA484, IA624) for 2 LAE with C IV candidates at $z_{\rm ph} = 3.002$, and (IA527, IA679) for 1 LAE with C IV candidate at $z_{\rm ph} = 3.346$. All of the 24 LAE candidates have $N_{\rm ex}^{\rm temp} = N_{\rm sol} = 2$.
[d] The LAE candidate have three excess IA-bands of IA484, IA505, and IA624. The first two excess IA-bands and IA624 band are considered to be caused by a single Lyα line and C IV line at $z_{\rm ph} = 3.073$. It has $N_{\rm ex}^{\rm temp} = N_{\rm sol} = 3$ and $\chi^2_\nu(z_{\rm ph}) = 2.24$.

Table 4
The Adopted Parameters in Our SED Fitting in Step 3.

Library	GALAXEV (Bruzual & Charlot 2003)
IMF	Chabrier (0.1–100 $M_\odot$)
Metallicity	0.0004, 0.004, 0.02 ($= Z_\odot$)
SFH	τ-model for $\tau = 0.01$–10 Gyr with interval of $\Delta\log(\tau/{\rm Gyr}) = 0.1$
Age	All age set of GALAXEV except for age $= 0$ yr[a]
Dust Extinction Law	Calzetti et al. (2000)
$E(B-V)$	0.0–1.5 with interval of $\Delta E(B-V) = 0.01$

[a] We also do not use the template older than cosmic age at $z_{\rm ph}$.

the LAE having two adjacent excess IA bands is not rejected in this step 4, the total number of the excess IA bands is 527 as shown in Table 5.

2.3. *Accuracy of Our Estimate for Photometric Redshift*

Before showing the properties of our LAE samples, we assess the quality of our $z_{\rm ph}$ estimate for our LAE samples through a comparison with their spectroscopic redshifts, $z_{\rm sp}$, using **xxx catalog**. We obtained $z_{\rm sp}$ for **xxx** LAEs from the catalog. We also searched $z_{\rm sp}$ for the other line emitters than Lyα (i.e., low-z emitters) in order to evaluate the fraction of mis-identification of emission line in our step 2; we found that **xxx** low-z emitters have $z_{\rm sp}$ which should be classfied as LAEs, i.e., $z_{\rm sp} =$ **2.5–5.8**.

Figure 4 shows the comparison between $z_{\rm ph}$ and $z_{\rm sp}$ for **xxx** LAEs and **xxx** low-z emitters.

- check whether or not $z_{\rm ph}$ of our LAE samples is consistent with $z_{\rm sp}$
- check the number of the low-z emitters classified by step 2 with $z_{\rm sp} = 2.5$–5.8

3. RESULTS

3.1. *Spatial Distribution*

We first show the spatial distribution of our 527 LAEs in the COSMOS field in Figure 5. For reference, we also present the spatial distributions of the LAEs at $z = 4.86$ and $z = 5.70$ selected by narrowband filters in the same COSMOS field (Shioya et al. 2009 for $z = 4.86$ LAEs and Murayama et al. 2007 for $z = 5.70$ LAEs) in Figure 6.

3.2. *Equivalent Width Distribution in Observer- and Rest-frame*

Then we investigate the EWs of our LAE samples. Figure 7 shows the $EW_{\rm obs}$ distribution for our 527 LAEs.

- check the relation between the selection criteria of

Table 5
Number of LAEs in Step 3 and Step 4 and of the LAEs with $EW_0 \geq 100$ Å.

IA-band	Number N									
	$N_{<5}$	$N_{\chi^2_\nu \leq 3}$	$N_{\rm Step\ 3}$	$N_{\rm IRAC}$	$N_{\rm Chandra}$	$N_{\rm XMM}$	$N_{\rm VLA}$	$N_{\rm AGN}$	$N_{\rm SFG}$	$N_{\rm sLAE}$
(1)	(2)	(3)	(4)	(5)	(6)	(7)	(8)	(9)	(10)	(11)
IA427	202	180	177	4	1	0	2	7	170	15
IA464	132	115	115	2	1	1	0	2[a]	113	15
IA484	262	241	239	9	11	1	1	17[b]	222	29
IA505	91	85	85	3	2	0	0	5	80	8
IA527	133	126	126	4	2	0	0	5	121	15
IA574	24	21	21	1	0	0	0	1	20	5
IA624	35	34	33	0	0	0	0	0	33	0
IA679	19	18	17	0	0	0	0	0	17	0
IA709	6	6	6	0	0	0	0	0	6	0
IA738	8	7	6	0	0	0	0	0	7	1
IA767	2	2	2	0	0	0	0	0	2	1
IA827	0	0	0	0	0	0	0	0	0	0
Total (excess IA-band)	914	835	827	23	17	2	3	37	791	89
Total (excess object)	895[c]	818[d]	811[e]	23	17[f]	2	3	37[f]	774[g]	88[h]

Note. — Col. (1): IA-band. Col. (2): Number of the LAE candidates having the number of the undetected IA-band filters whose effective wavelengths are longer than the redshifted Lyα wavelength less than 5. Col. (3): Number of the LAE candidates satisfying $\chi^2_\nu(z_{\rm ph}) \leq 3$ out of $N_{<5}$. Col. (4): Number of the LAE candidates selected via Step 3. Col. (5): Number of the LAE candidates satisfying the IRAC color criteria proposed by Donley et al. (2012) out of $N_{\rm Step\ 3}$. Col. (6): Number of the LAE candidates detected with Chandra within 1 arcsec out of $N_{\rm Step\ 3}$. Col. (7): Number of the LAE candidates detected with XMM-Newton within its error circle out of $N_{\rm Step\ 3}$. Col. (8): Number of the LAE candidates detected with VLA within a radius of 1 arcsec out of $N_{\rm Step\ 3}$. Col. (9) Number of the LAE candidates classified as AGN, which is the logical sum of $N_{\rm IRAC}$, $N_{\rm Chandra}$, $N_{\rm XMM}$, and $N_{\rm VLA}$. Col. (10): Number of our sample of star-forming LAE, which is calculated via $N_{\rm Step\ 3} - N_{\rm AGN}$. Col. (11): Number of our sample of the LAE with rest-frame EW of $EW_0 \geq 100$ Å, which is called as strong LAE in this paper (see Section 3.2).

[a] The one Chandra source is also rejected by the IRAC color criteria and detected by the XMM-Newton. Therefore, the number of AGNs here is 4.

[b] While there is no overlap among the IRAC, XMM-Newton, and the VLA selected AGNs, three out of the eleven Chandra sources are also rejected by the IRAC color criteria. Moreover, the two XMM-Newton sources and the one VLA souce are also detected as Chandra sources. Therefore, the number of AGNs here is 17.

[c] 108 LAE candidates in Step 2 are rejected by this criteria and all of them are the LAE candidates with $N_{\rm ex}^{\rm cons} = 1$. All of the 27 LAE candidates with $N_{\rm ex}^{\rm cons} > 1$ in Step 2 are included here.

[d] 59, 7, and 1 LAE candidates with $N_{\rm ex}^{\rm cons} = 1$, 2, and 3 in Step 2, respectively, are rejected by this criteria. Out of the 683 LAE candidates, nineteeen candidates are with $N_{\rm ex}^{\rm cons} = 2$. Seventeen LAE candidates have two adjacent excess IA-bands, which are considered to be caused by a single Lyα line. The combinations of the two excess IA-bands for these LAE candidates are the following: (IA464, IA484) for 1 LAE candidate at $z_{\rm ph} = 2.896$, (IA484, IA505) for 3 LAE candidates at $z_{\rm ph} = 3.073$, (IA505, IA527) for 11 LAE candidates at $z_{\rm ph} = 3.241$, (IA679, IA709) for 1 LAE candidate at $z_{\rm ph} = 4.699$, and (IA709, IA738) for 1 LAE candidate at $z_{\rm ph} = 4.931$. The other 2 LAE candidates have two separated excess IA-bands, which are considered to be caused by Lyα and C III]. The combinations of two excess IA-bands for these LAE with C III] candidates are the following: (IA464, IA709) for 1 LAE with C III] candidate at $z_{\rm ph} = 2.754$ and (IA464, IA738) for 1 LAE with C III] candidate at $z_{\rm ph} = 2.835$.

[e] 94 and 1 LAE candidates with $N_{\rm ex}^{\rm cons} = 1$ and 2, respectively, are rejected by this criteria. Out of the 588 LAEs, eighteen LAEs are with $N_{\rm ex}^{\rm cons} = 2$. **Among them, xxx have $N_{\rm ex} = 2$.**

[f] An LAE with $N_{\rm ex} = 2$ selected both in IA484 and IA505 bands is detected in the Chandra source catalog.

[g] **Since an LAE having two excess IA-bands is rejected as possibly AGN-powered LAE, the twelve LAEs with $N_{\rm ex} = 2$ are included in our star-forming LAE samples.**

[h] Two LAEs have the two excess IA-bands of IA505 and IA527 from which EW_0 are evaluated as ≥ 100 Å.

$EW_{\rm obs} \gtrsim 150$ Å and the resultant $EW_{\rm obs}$ distributions of our 527 LAEs

- assess the dependence of the resultant threshold of $EW_{\rm obs}$, $EW_{\rm obs}^{\rm th}$ on redshift; it is expected that $EW_{\rm obs}^{\rm th}$ increases with redshift because the criteria for the EW significance is more severe for higher-z faint sources

Figure 8 shows the distributions of the rest-frame EW, EW_0, for our 527 LAEs. Among the 527 LAEs identified through the procedures described in the previous section, 63 LAEs are found to have very strong Lyα emissions of $EW_0 \geq 100$ Å as shown in Figure 8. We call these LAEs as strong LAEs hereafter.

3.3. *Distribution in L(Lyα) and EW_0–L(Lyα) Plane*

- check the properties of our LAE sample through the distributions in L(Lyα) and in EW_0–L(Lyα)

3.4. *Dependence of EW_0 on sSFR and $M_\star$*

- it is expected that EW_0 does depend on $sSFR$ but do not depend on $M_\star$
- the errors in SFR seem to be terribly large <– this could be caused by a combination of extremely small e-folding time τ (< 0.1 Gyr) and young age; small changes in τ and age can result in a significant change in SFR
  –> it may be better that SFR is evaluated from the rest-frame UV continuum luminosity of the best-fit SED model and $E(B-V)$ from the SED fitting result; check the distribution in age–τ plane

3.5. *Distribution in SFR–EW_0 Plane*

- it is expected that more massive samples have smaller $sSFR$

4. DISCUSSION

4.1. *Median SEDs*

5. CONCLUSIONS

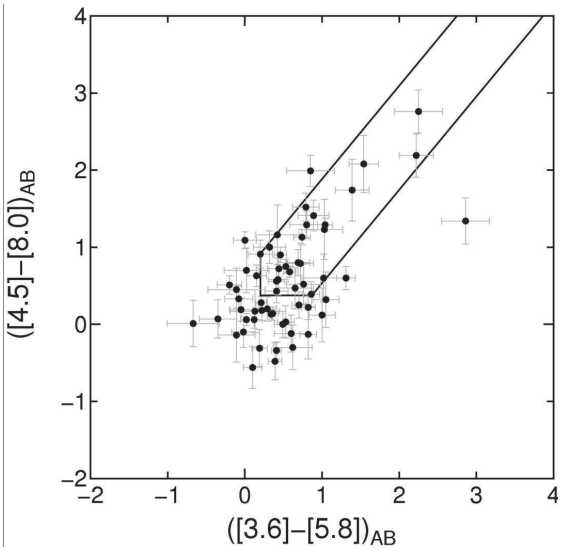

Figure 3. **(Replace this figure into the one in which all LAEs detected in all of the four IRAC bands are plotted and in which the area of Donley+12 criteria are shown as gray-colored.) [3.6] − [5.8] vs. [4.5] − [8.0] diagram for the xxx LAEs detected in all of the four IRAC bands. The red-filled and blue-filled circles represent the LAEs with $EW_0 < 100$ Å and $EW_0 \geq 100$ Å, respectively. The criteria proposed by Donley et al. (2012) are shown by the solid lines. The 25 LAEs in the gray-colored region are rejected as AGN candidates.**

We would like to thank both the Subaru and HST staff for their invaluable help, and all members of the COSMOS team.

REFERENCES

Bouwens, R. J., Illingworth, G. D., Labbe, I., et al. 2011, Nature, 469, 504
Brammer, G. B., van Dokkum, P. G., & Coppi, P. 2008, ApJ, 686, 1503
Bruzual, G., & Charlot, S. 2003, MNRAS, 344, 1000
Cardamone, C., Schawinski, K., Sarzi, M., et al. 2009, MNRAS, 399, 1191
Chabrier, G. 2003, PASP, 115, 763
Cowie, L. L., Songaila, A., Hu, E. M., & Cohen, J. G. 1996, AJ, 112, 839
Donley, J. L., Koekemoer, A. M., Brusa, M., et al. 2012, ApJ, 748, 142
Hagen, A., Ciardullo, R., Gronwall, C., et al. 2014, ApJ, 786, 59
Hasinger, G., Cappelluti, N., Brunner, H., et al. 2007, ApJS, 172, 29
Hu, E. M., Cowie, L. L., McMahon, R. G., et al. 2002, ApJ, 568, L75
Huang, X., Zheng, W., Wang, J., et al. 2015, ApJ, 801, 12
Ilbert, O., Capak, P., Salvato, M., et al. 2009, ApJ, 690, 1236
Ilbert, O., McCracken, H. J., Le Fèvre, O., et al. 2013, A&A, 556, A55
Konno, A., Ouchi, M., Ono, Y., et al. 2014, ApJ, 797, 16
Kunth, D., Mas-Hesse, J. M., Terlevich, E., et al. 1998, A&A, 334, 11
Massey, R., Rhodes, J., Ellis, R., et al. 2007, Nature, 445, 286
McCracken, H. J., Milvang-Jensen, B., Dunlop, J., et al. 2012, A&A, 544, A156
Meier, D. L. 1976, ApJ, 207, 343
Mori, M., & Umemura, M. 2006, Nature, 440, 644
Murayama, T., Taniguchi, Y., Scoville, N. Z., et al. 2007, ApJS, 172, 523
Ono, Y., Ouchi, M., Shimasaku, K., et al. 2010, MNRAS, 402, 1580
Ouchi, M., Shimasaku, K., Akiyama, M., et al. 2008, ApJS, 176, 301
Partridge, R. B., & Peebles, P. J. E. 1967, ApJ, 147, 868
Peng, C. Y., Ho, L. C., Impey, C. D., & Rix, H.-W. 2002, AJ, 124, 266
Pérez-González, P. G., Rieke, G. H., Villar, V., et al. 2008, ApJ, 675, 234
Sanders, D. B., Salvato, M., Aussel, H., et al. 2007, ApJS, 172, 86
Schaerer, D. 2003, A&A, 397, 527
Schinnerer, E., Smolčić, V., Carilli, C. L., et al. 2007, ApJS, 172, 46
Scoville, N., Aussel, H., Brusa, M., et al. 2007, ApJS, 172, 1
Shioya, Y., Taniguchi, Y., Sasaki, S. S., et al. 2009, ApJ, 696, 546
Taniguchi, Y., Ajiki, M., Nagao, T., et al. 2005, PASJ, 57, 165
Taniguchi, Y., Scoville, N., Murayama, T., et al. 2007, ApJS, 172, 9
Taniguchi, Y., Shioya, Y., & Trump, J. R. 2010, ApJ, 724, 1480
van der Wel, A., Franx, M., van Dokkum, P. G., et al. 2014, ApJ, 788, 28

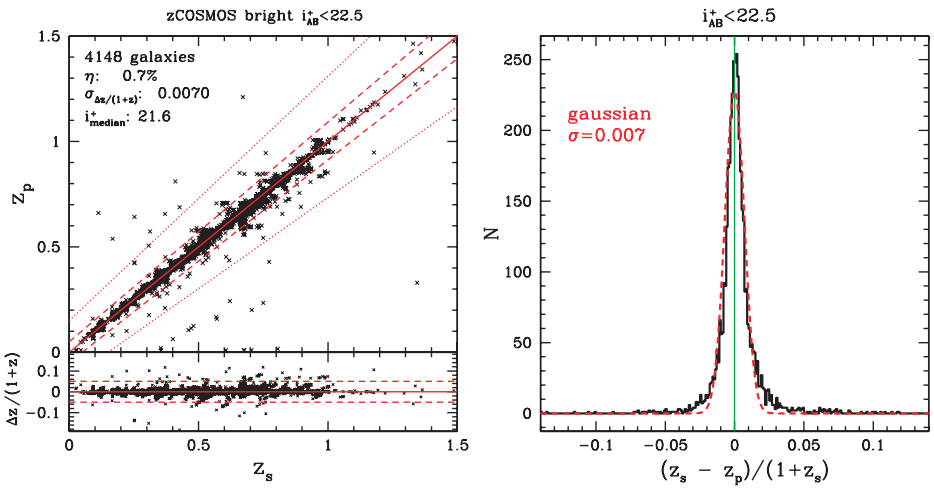

Figure 6. Left panel: comparison between $z_{\rm p}$ and $z_{\rm s}$ for the bright spectroscopic selected sample $17.5 \leqslant i^{+}_{\rm AB} \leqslant 22.5$ (zCOSMOS-bright; S. J. Lilly et al. 2008, in preparation). The dotted and dashed lines are for $z_{\rm p} = z_{\rm s} \pm 0.15(1+z_{\rm s})$ and $z_{\rm p} = z_{\rm s} \pm 0.05(1+z_{\rm s})$, respectively. The 1σ dispersion, the fraction of catastrophic failures and the median apparent magnitude are listed in the top-left corner of the left panel. Right panel: $\Delta z/(1+z_{\rm s})$ distribution. The dashed line is a Gaussian distribution with $\sigma = 0.007$.

Figure 4. **(Replace this Figure (Fig. 6 of Ilbert+09) into the adequate one in the format like this figure) *Left*: Comparison between the spectroscopic redshift $z_{\rm sp}$ and our estimate of $z_{\rm ph}$. The blue-filled circles and red-open triangles are the 39 LAEs and the xxx low-z emitters with $z_{\rm sp}$, respectively. The solid line represents the one-to-one correspondence between $z_{\rm ph}$ and $z_{\rm sp}$. On the other hand, the dashed and dotted lines are for $z_{\rm ph} = z_{\rm sp} \pm 0.15(1+z_{\rm sp})$ and $z_{\rm ph} = z_{\rm sp} \pm 0.05(1+z_{\rm sp})$, respectively. *Right*: Distribution of $\Delta z/(1+z_{\rm sp})$. The dashed line is a Gaussian distribution with $\sigma = xxx$.**

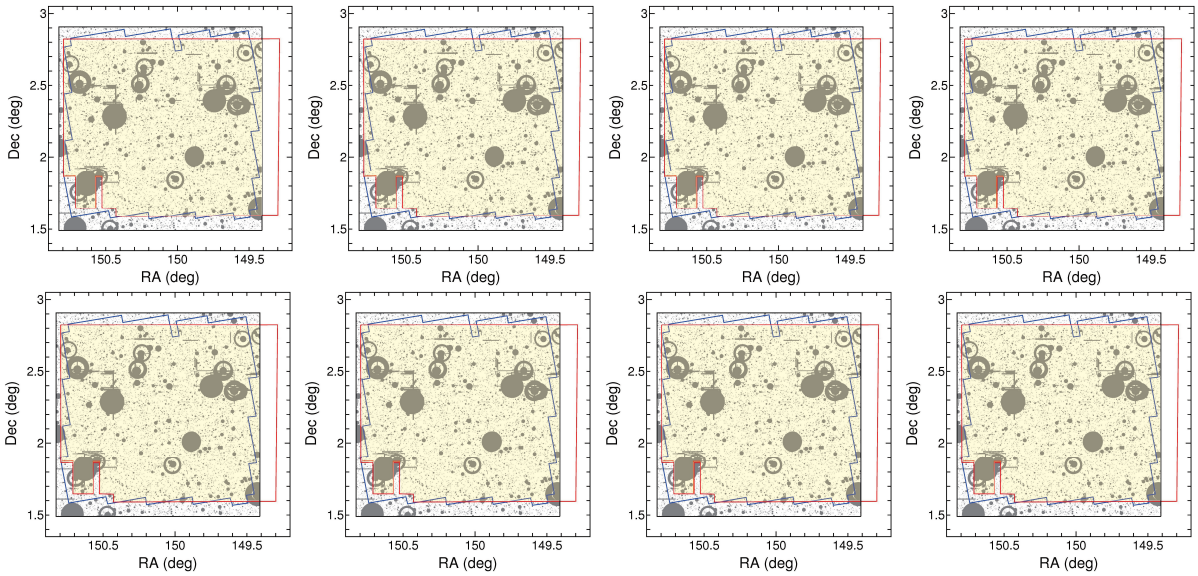

Figure 5. **(Insert here) Spatial distributions of our final sample of LAEs in the COSMOS 2-square degree field. In each panel, the red- and blue-filled circles show the LAEs with $EW_0 < 100$ Å and $EW_0 \geq 100$ Å, respectively. The COSMOS deep area, the UltraVISTA area, and the HST/ACS area are shown by black, red, and blue lines, respectively. The grey-shaded regions are the areas masked out for the detection. The xxx LAEs showing two-adjacent IA-band excess are plotted in the corresponding two panels.**

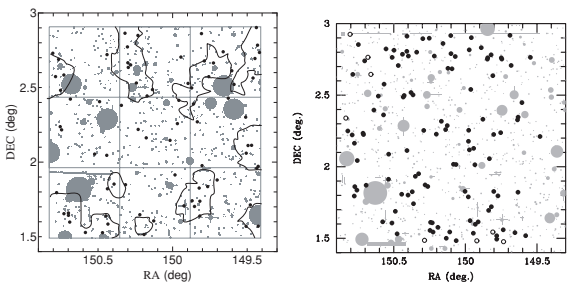

Figure 6. **(Replace this into the figure in same format.) Spatial distributions of the narrowband-selected LAEs at $z = 4.86$ (left) and $z = 5.70$ (right) in the COSMOS field. Symbols are the same as those in Figure 5.**

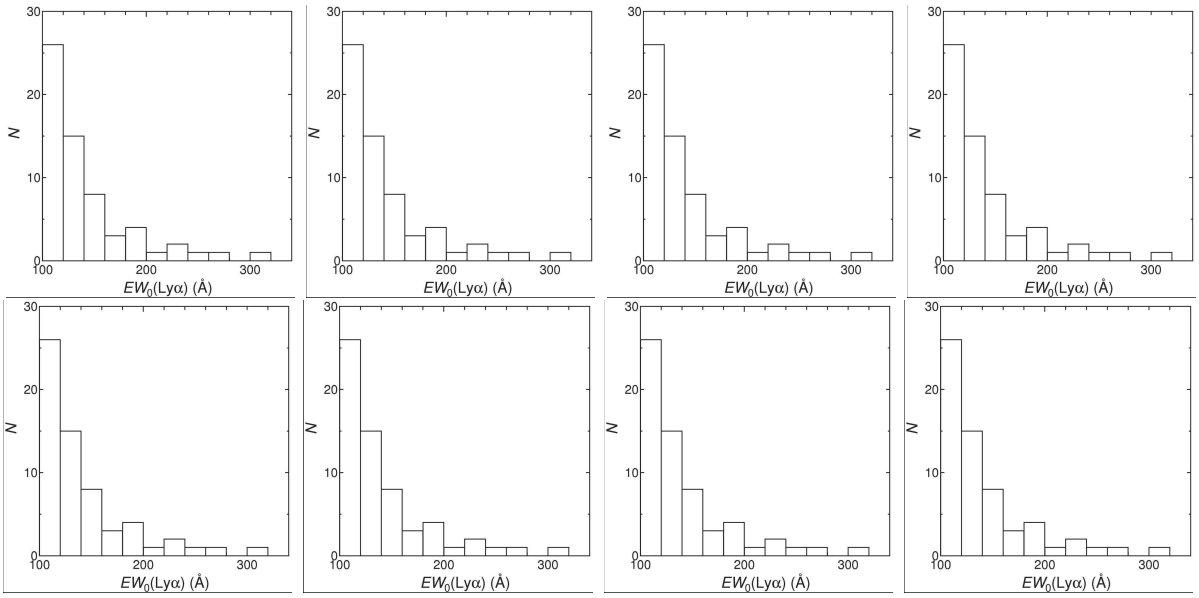

Figure 7. **(Replacing this figure into the EW_{obs} distributions for 527 LAEs. Each IA-band selected LAEs are separately shown in 4 × 2 panels. In each panel, the IA-band and the corresponding z_{ph} are displayed on the top left.) EW_{obs} distributions for our 527 LAEs. The LAEs selected in each IA-band are separately presented in each panel. The vertical dashed line represent $EW = 150$ Å, which roughly corresponds to our selection criteria of Equation (1).**

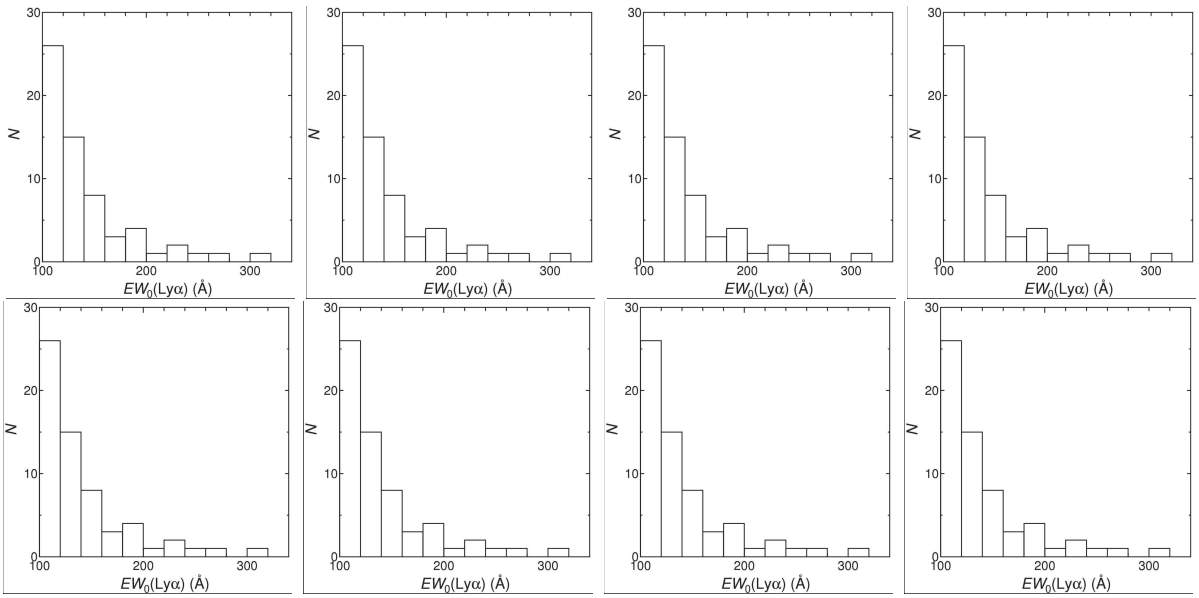

Figure 8. **(Replacing this figure into the EW_0 distributions for 527 LAEs. Same format as that of Figure 7) Same as Figure 7, but for EW_0 distributions. The solid histogram shows the EW_0 distribution of the corresponding IA-band selected LAEs. The EW_0 distribution of all 527 LAEs are also shown in each panel by the gray histogram, which is normalized so that the total number is matched to that of the corresponding IA-band selected LAEs.**

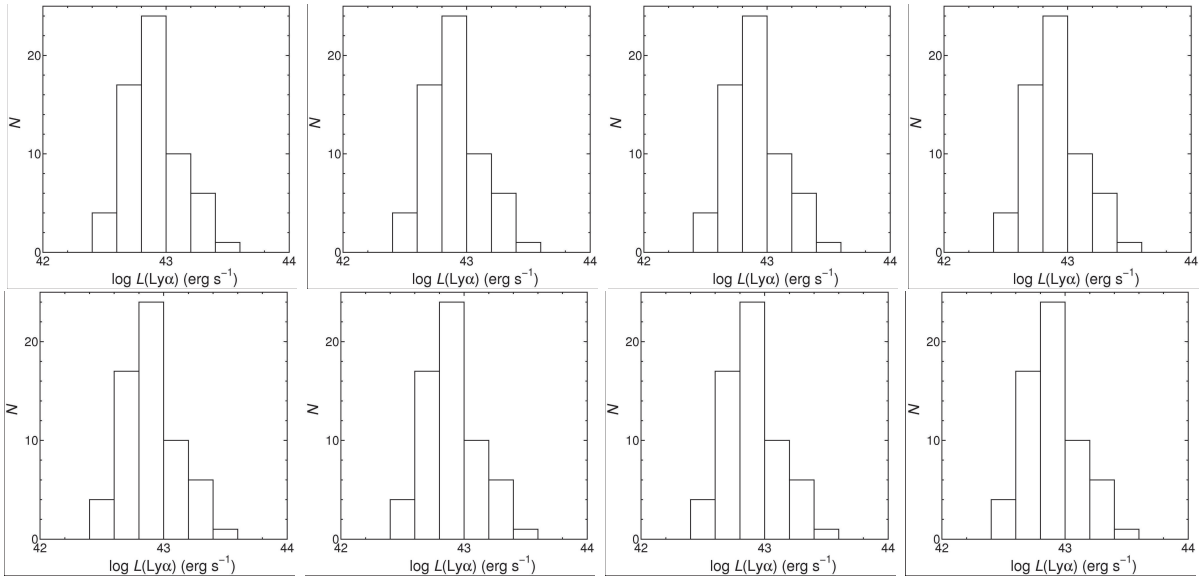

Figure 9. **(Replacing this into the figure with 4 × 2 panels for each IA-band selected LAEs + all LAEs in the bottom right. Labels of the IA-band and $z_{\rm ph}$ are shown at the top left in each panel. Vertical axis should be N itself not the volume density n) Same as Figure 7, but for $L(\mathrm{Ly}\alpha)$ distribution.**

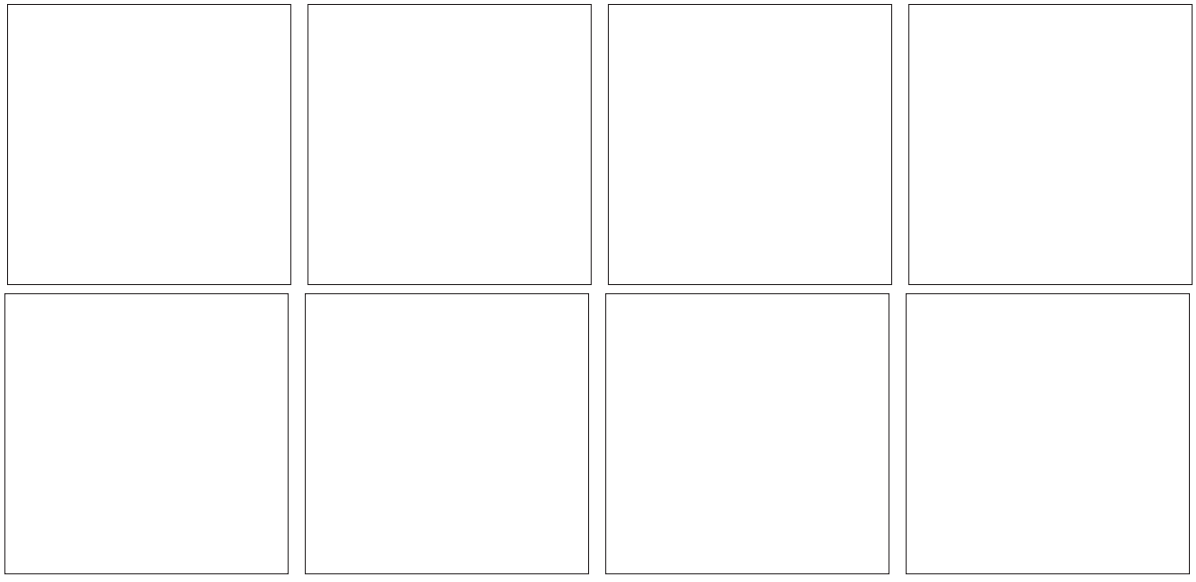

Figure 10. **(Insert here. 4 × 2 panels for each IA-band selected LAEs.) Distribution of 527 LAEs in the EW_0–$L(\mathrm{Ly}\alpha)$ plane. The red- and blue-filled circles show the LAEs with $EW_0 < 100$ Å and $EW_0 \geq 100$ Å, respectively.**

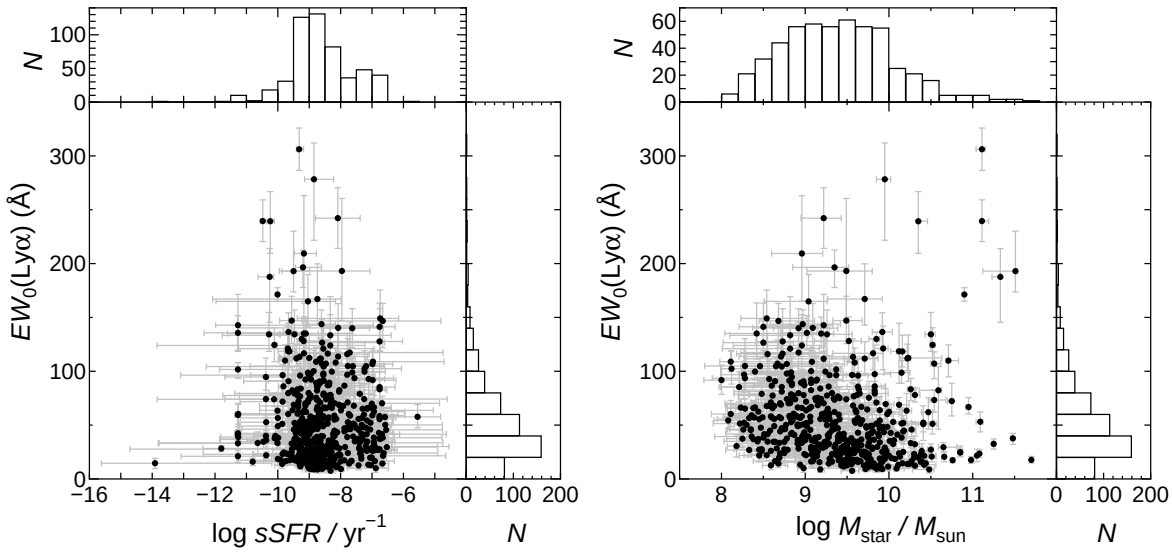

Figure 11. *Left*: Distribution of LAEs in the EW_0–$sSFR$ plane. **(the histogram of SSFR is revised for the one which the probability distribution of SSFR for each LAE is incorporated.)** *Right*: Same as left panel, but for the distribution in the EW_0–$M_\star$ plane.

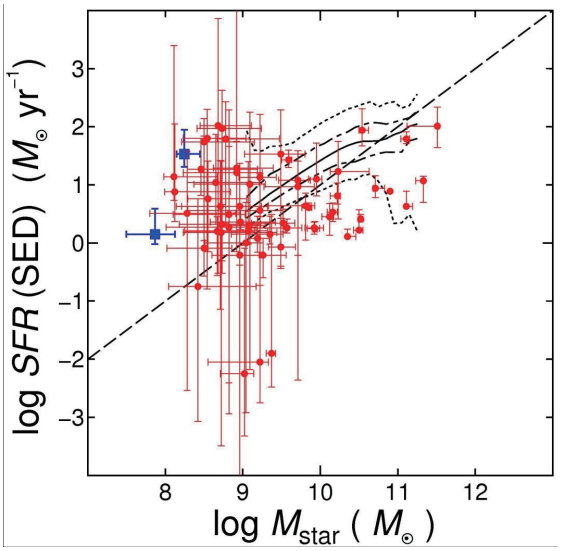

Figure 12. **(Replace this into the figure in which all LAEs are plotted.) Distribution of LAEs in the SFR(SED) vs. $M_\star$ plane. The red- and blue-filled circles show the LAEs with $EW_0 < 100$ Å and $EW_0 \geq 100$ Å, respectively. We also present the distribution of the galaxies at $z_{\rm ph} = 2.5$–3.8 in the COSMOS field in gray scale with bin size of 0.1 dex both in $M_\star$ and SFR for reference. The scale (the number of galaxies per bin) is shown in the upper-left inset. The solid, dot-dashed, and dotted curves represent the median, 16- and 84-percentiles, and 2.5- and 97.5 percentiles in bins of 0.1 dex in $M_\star$. The dashed line shows the relation of $sSFR = 1$ Gyr^{-1}.**

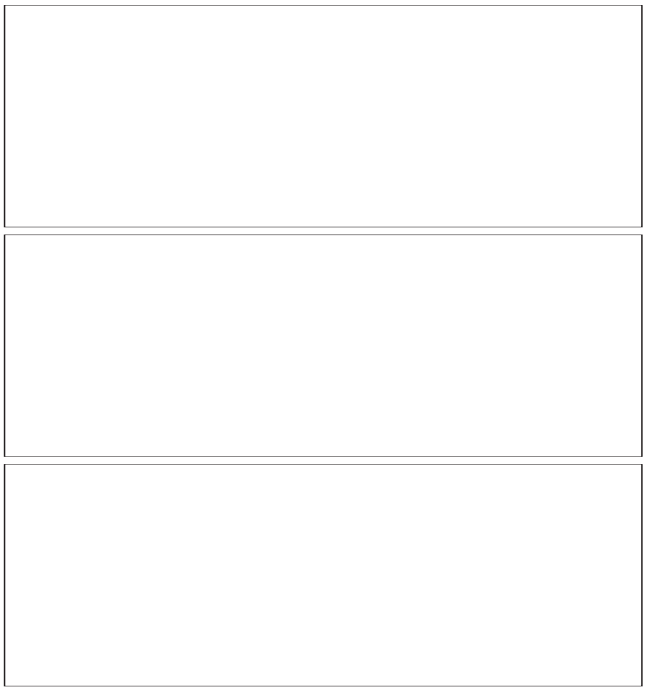

Figure 13. **(Insert here. 1×3 panels for the sFR distributions of the LAEs with $\log(M_\star/M_\odot) \geq 10.5$ (top), 9.5–10.5 (middle), and < 9.5 (bottom). The corresponding mass range is shown at the top left and the number of the LAEs at the top right. In each panel, distributions of all samples are shown in open histogram while those of the LAEs with $EW_0 \geq 100$ Å are shown in filled histogram.) Distribution of LAEs in sFR.**

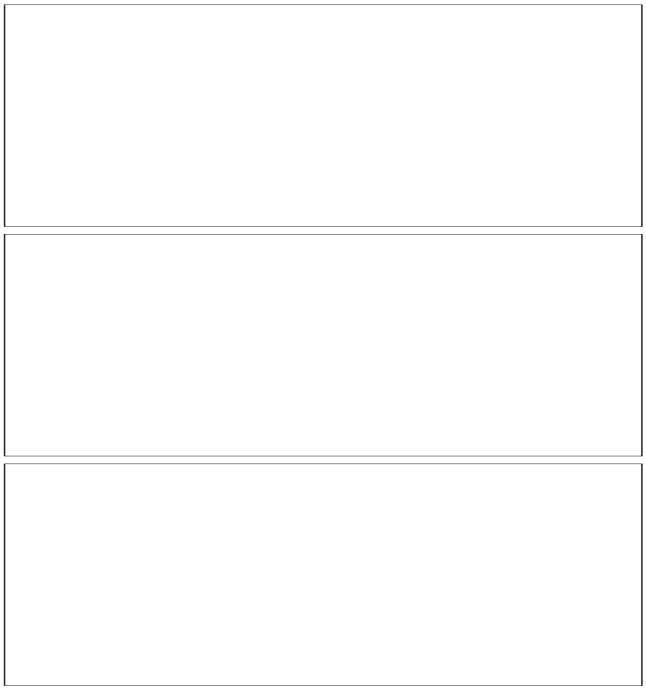

Figure 14. **(Insert the figure with $f_\nu/f_\nu(\lambda = 1350\ )$ vs. λ_0 here. 1×3 panels for the SEDs of the 9 MAESTLOs (top), 63 LAEs with $EW_0 \geq 100$ Å (middle), and all LAEs (bottom). The corresponding label is shown at the top left and the number of the LAEs at the top right. In each panel, the observed data points of all sources are shown in grey data points without error and the best-fit SED model is shown by the solid curve. The best-fit SED is evaluated via the fits to all observed data assuming an equal weight.) Comparison of the rest-frame SED between the MAESTLO, strong LAEs, and all LAEs.**

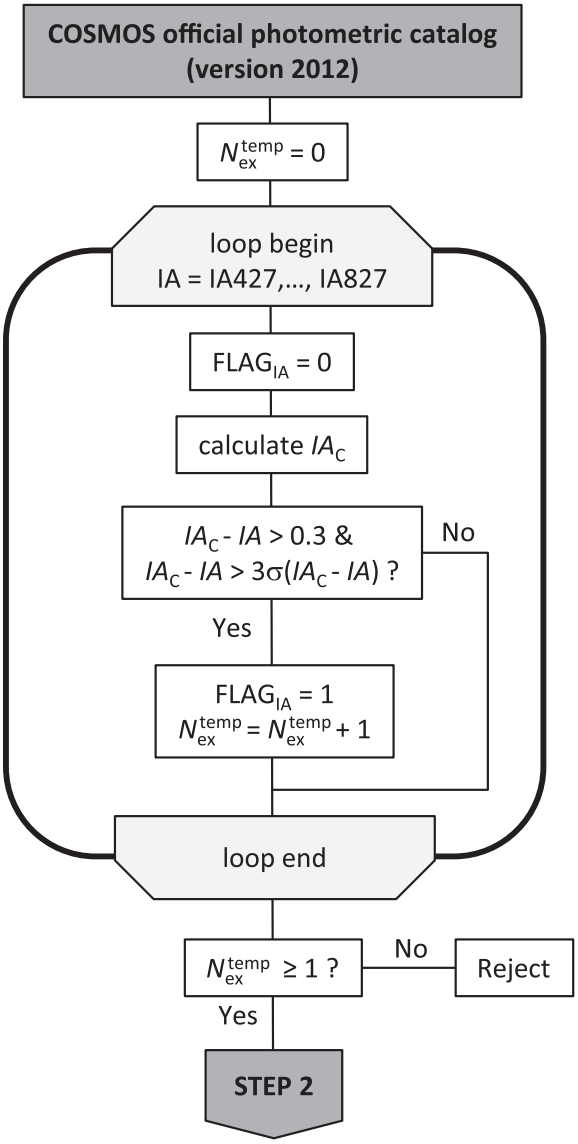

Figure A1. Flowchart for the Step 1. Note that this flowchart is for a single object in the catalog; all objects in the catalog go along this flowchart independently. See Table A1 for the definition of the variables used here.

APPENDIX

A. DETAILS OF OUR PROCEDURES TO SELECT LAES

A.1. *Step 1: Selection of IA-band excess objects*

A.2. *Step 2: Selection of LAE candidates*

A.3. *Step 3: Selection of real LAEs*

A.4. *Step 4: Rejection of possibly AGN-powered LAEs*

B. SPECTRAL ENERGY DISTRIBUTIONS OF THE STRONG LAES

The observed SEDs and thumbnails of the 63 strong LAEs are shown in Figure B1.

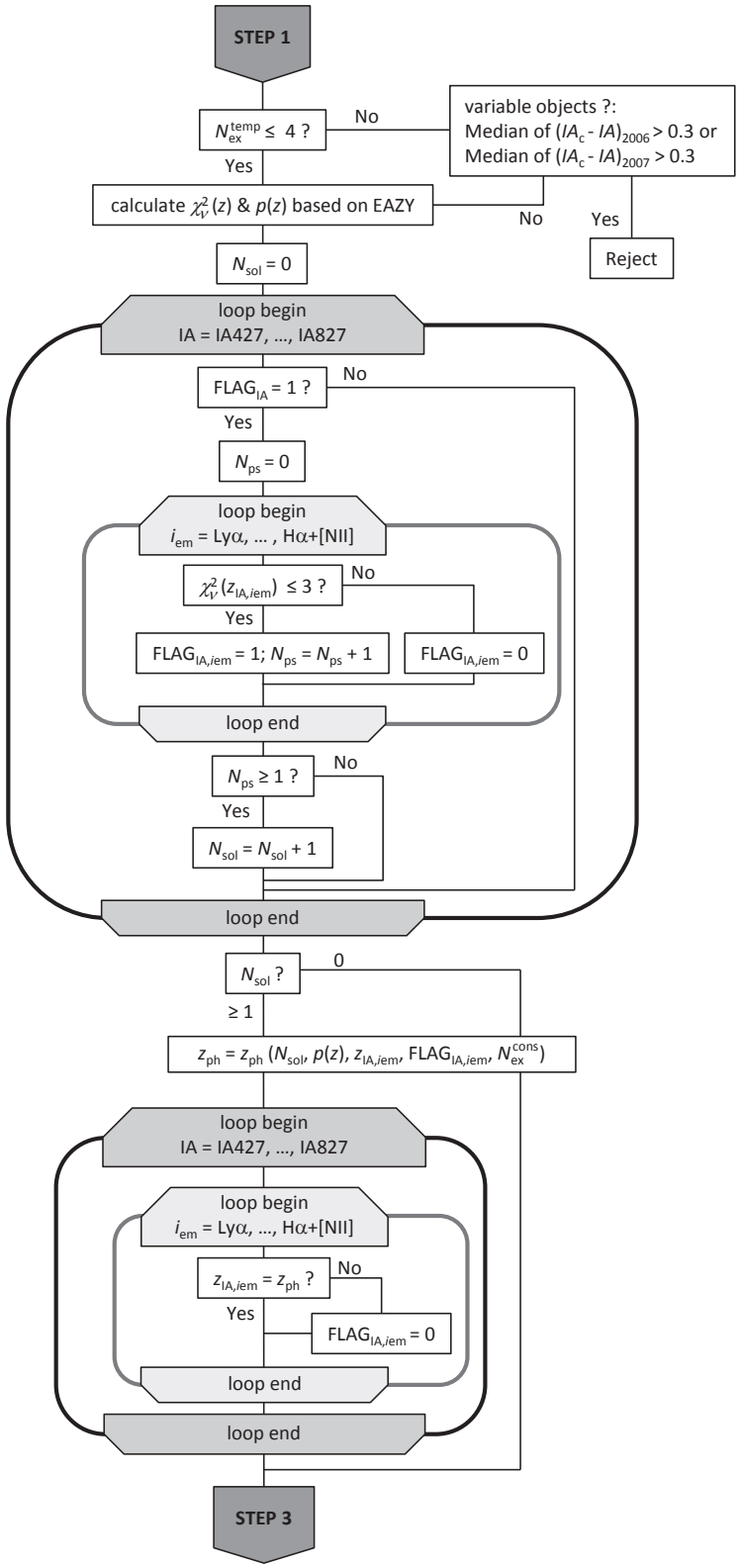

Figure A2. Same as Figure A1, but for flowchart for the Step 2. See Table A1 for the definition of the variables used here.

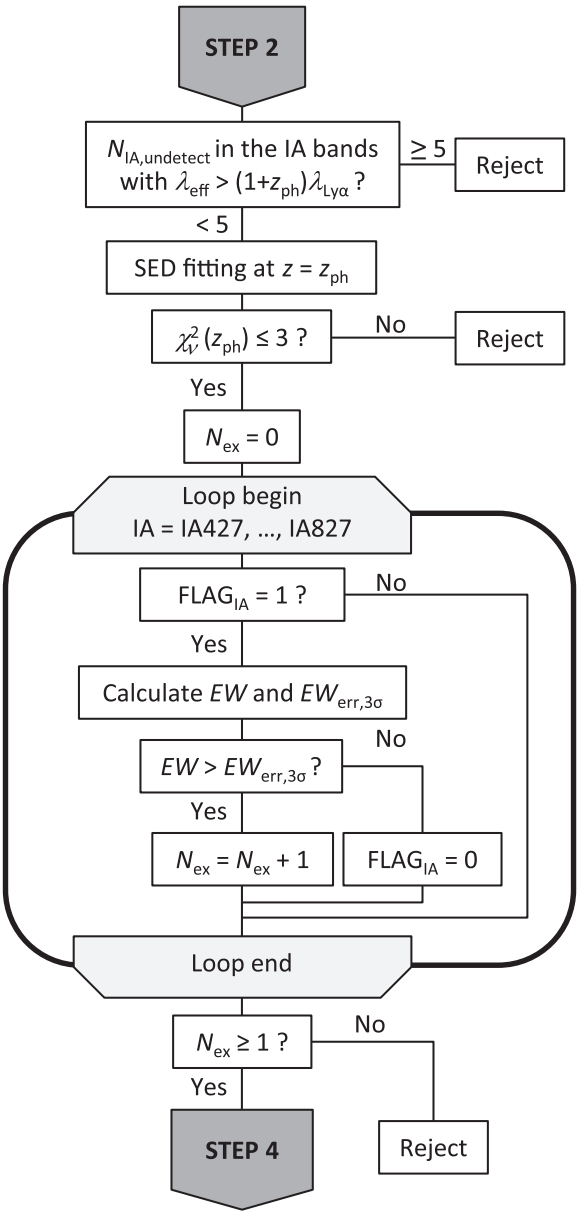

Figure A3. Same as Figure A1, but for flowchart for the Step 3. See Table A1 for the definition of the variables used here.

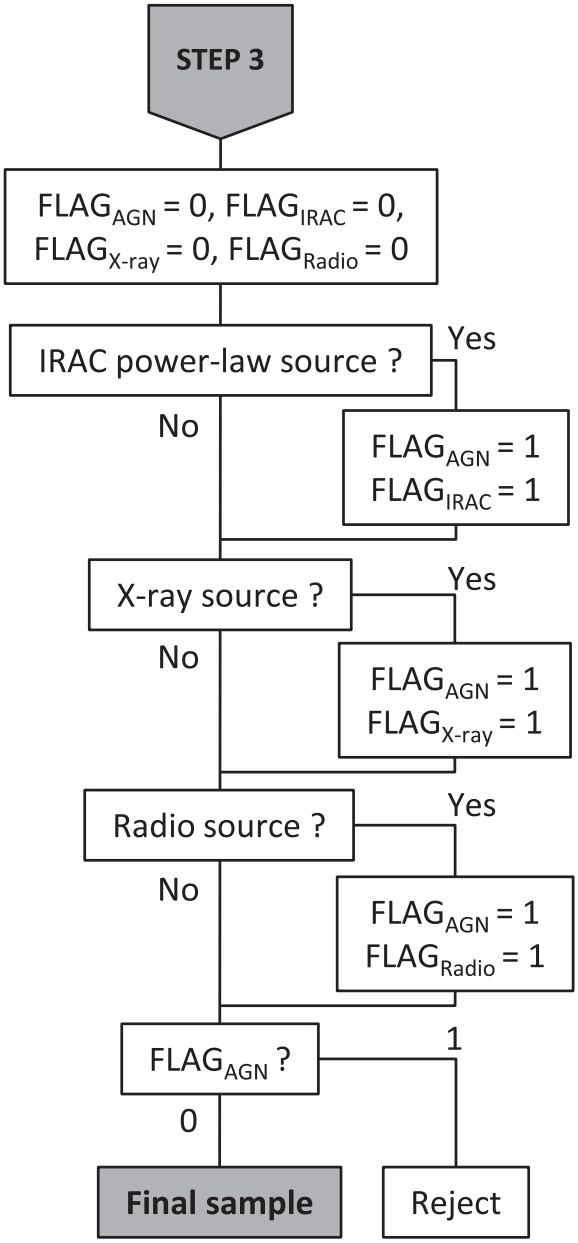

Figure A4. Same as Figure A1, but for flowchart for the Step 4. See Table A1 for the definition of the variables used here.

Table A1
Definition of the variables used in our flowcharts for Step 1 to Step 4.

Symbol	Note
Step 1	
$N_{\rm ex}^{\rm temp}$	Number of the excess IA-bands which satisfy the criteria of Equations (1) and (2)[a]
$\rm FLAG_{IA}$	Flag for the excess IA-band[b]
Step 2	
$(IA_{\rm c}-IA)_{2006}$	$IA_{\rm c}-IA$ for the IA bands observed during a period between 2006 January and 2006 February (i.e., IA427, IA464, IA505, IA574, IA679, IA709, and IA827)
$(IA_{\rm c}-IA)_{2007}$	$IA_{\rm c}-IA$ for the IA bands observed during a period between 2006 December and 2007 March (i.e., IA484, IA527, IA624, IA738, and IA767)
$\chi^2_\nu(z)$	Reduced χ-square as a function of redshift z
$p(z)$	Volume-weighted likelihood as a function of redshift z
$z_{{\rm IA},i{\rm em}}$	Redshift expected for emission line $i_{\rm em}$ redshifted into the IA bandpass[c]
$N_{\rm ps}$	Number of emission lines which satisfies $\chi^2_\nu(z_{{\rm IA},i{\rm em}})\leq 3$ (ps = possible solution)[d]
$N_{\rm sol}$	Number of the excess IA-bands having at least one emission line $i_{\rm em}$ which satisfies $\chi^2_\nu(z_{{\rm IA},i{\rm em}})\leq 3$[e]
$\rm FLAG_{IA,\mathit{i}em}$	Flag for the excess IA-band satisfying $\chi^2_\nu(z_{{\rm IA},i{\rm em}})\leq 3$ for emission line $i_{\rm em}$[f]
$N_{\rm ex}^{\rm cons}$	Maximum number of emission lines which have a consistent solution of redshift among $N_{\rm sol}$'s line identification[g]
$z_{\rm ph}(N_{\rm sol},p(z),z_{{\rm IA},i{\rm em}},{\rm FLAG}_{{\rm IA},i{\rm em}},N_{\rm ex}^{\rm cons})$	Photometric redshift determined by $N_{\rm sol}$, $p(z)$, $z_{{\rm IA},i{\rm em}}$, $\rm FLAG_{IA,\mathit{i}em}$, and $N_{\rm ex}^{\rm cons}$ [h]
Step 3	
$N_{\rm IA,undetect}$	Number of the undetected IA bands among the IA bands whose effective wavelength is longer than the redshifted Lyα wavelength of $(1+z_{\rm ph})\lambda_{{\rm Ly}\alpha}$
$N_{\rm ex}$	Number of the IA excess bands satisfying both of $\chi^2_\nu(z_{\rm ph})\leq 3$ and $EW>EW_{{\rm err},3\sigma}$
Step 4	
$\rm FLAG_{IRAC}$	Flag for the LAE possibly powered by AGN according to its IRAC color[i]
$\rm FLAG_{X\text{-}ray}$	Flag for the LAE possibly powered by AGN according to its X-ray flux[j]
$\rm FLAG_{Radio}$	Flag for the LAE possibly powered by AGN according to its radio flux[k]
$\rm FLAG_{AGN}$	Flag for the LAE possibly powered by AGN[l]

[a] $N_{\rm ex}^{\rm temp}$ is counted in Step 1 and used in Step 2.

[b] We set $\rm FLAG_{IA}$ only for the excess IA-band as unity. This flag is used in Steps 2 and 3.

[c] $z_{{\rm IA},i{\rm em}}$ is determined by the rest-frame frequency of the emission line $i_{\rm em}$ and the bandpass of the IA-band; therefore, $z_{{\rm IA},i{\rm em}}$ is not a unified value but represents a range of redshift for a certain combination of IA band and emission line. This variable is used only in Step 2.

[d] $N_{\rm ps}$ is temporal variable defined for individual IA band and used only to judge whether or not there is at least one emission line $i_{\rm em}$ satisfying $\chi^2_\nu(z_{{\rm IA},i{\rm em}})\leq 3$ in Step 2.

[e] $N_{\rm sol}$ is used only to determine the photometric redshift of the line emitter candidate $z_{\rm ph}$ in Step 2. The magnitude relation between $N_{\rm sol}$ and $N_{\rm ex}^{\rm temp}$ is $N_{\rm sol}\leq N_{\rm ex}^{\rm temp}$ for all IA-excess candidates by definition.

[f] We set $\rm FLAG_{IA,\mathit{i}em}$ as unity only for the excess IA-band satisfying $\chi^2_\nu(z_{{\rm IA},i{\rm em}})\leq 3$ for emission line $i_{\rm em}$. This flag is used to determine $z_{\rm ph}$ in Steps 2 and to classify the line emitter candidate.

[g] $N_{\rm ex}^{\rm cons}$ is determined in the process of determination of $z_{\rm ph}$. The magnitude relation between $N_{\rm ex}^{\rm cons}$ and $N_{\rm sol}$ is $N_{\rm ex}^{\rm cons}\leq N_{\rm sol}$ ($\leq N_{\rm ex}^{\rm temp}$) for all IA-excess candidates by definition.

[h] $z_{\rm ph}$ is determined using the quantities of $N_{\rm sol}$, $p(z)$, $z_{{\rm IA},i{\rm em}}$, and $\rm FLAG_{IA,\mathit{i}em}$ as follows. (1) For the line emitter candidates with $N_{\rm sol}=0$, $z_{\rm ph}$ is adopted to be the redshift at which $p(z)$ is the maximum. Note that, in this procedure, we do not consider whether or not the condition of $\chi^2_\nu(z_{\rm ph})\leq 3$ is satisfied. (2) For those with $N_{\rm sol}=1$, we adopt $z_{\rm ph}$ as the arithmetic mean of $z_{{\rm IA},i{\rm em}}$ which satisfies $\rm FLAG_{IA,\mathit{i}em}=1$. (3) For those with $N_{\rm sol}\geq 2$, $z_{\rm ph}$ is adopted to be the arithmetic mean of the redshift range in which the number of excess IA-bands caused by the considered emission lines becomes the maximum, $N_{\rm ex}^{\rm cons}$. If there are several solutions at the same $N_{\rm ex}^{\rm cons}$, $z_{\rm ph}$ is adopted to be the redshift at which $p(z)$ is largest.

[i] $\rm FLAG_{IRAC}=1$ is assigned only to the LAEs satisfying the IRAC color criteria proposed by Donley et al. (2012).

[j] $\rm FLAG_{X\text{-}ray}=1$ is assigned only to the LAEs detected by either Chandra or XMM-Newton within an error circle using the new Chandra-COSMOS catalog and XMM-COSMOS database.

[k] $\rm FLAG_{Radio}=1$ is assigned only to the LAEs detected by VLA within a radius of 1 arcsec using the VLA-COSMOS database.

[l] We adopt $\rm FLAG_{AGN}=1$ for the LAEs having either $\rm FLAG_{IRAC}=1$, $\rm FLAG_{X\text{-}ray}=1$, or $\rm FLAG_{Radio}=1$.

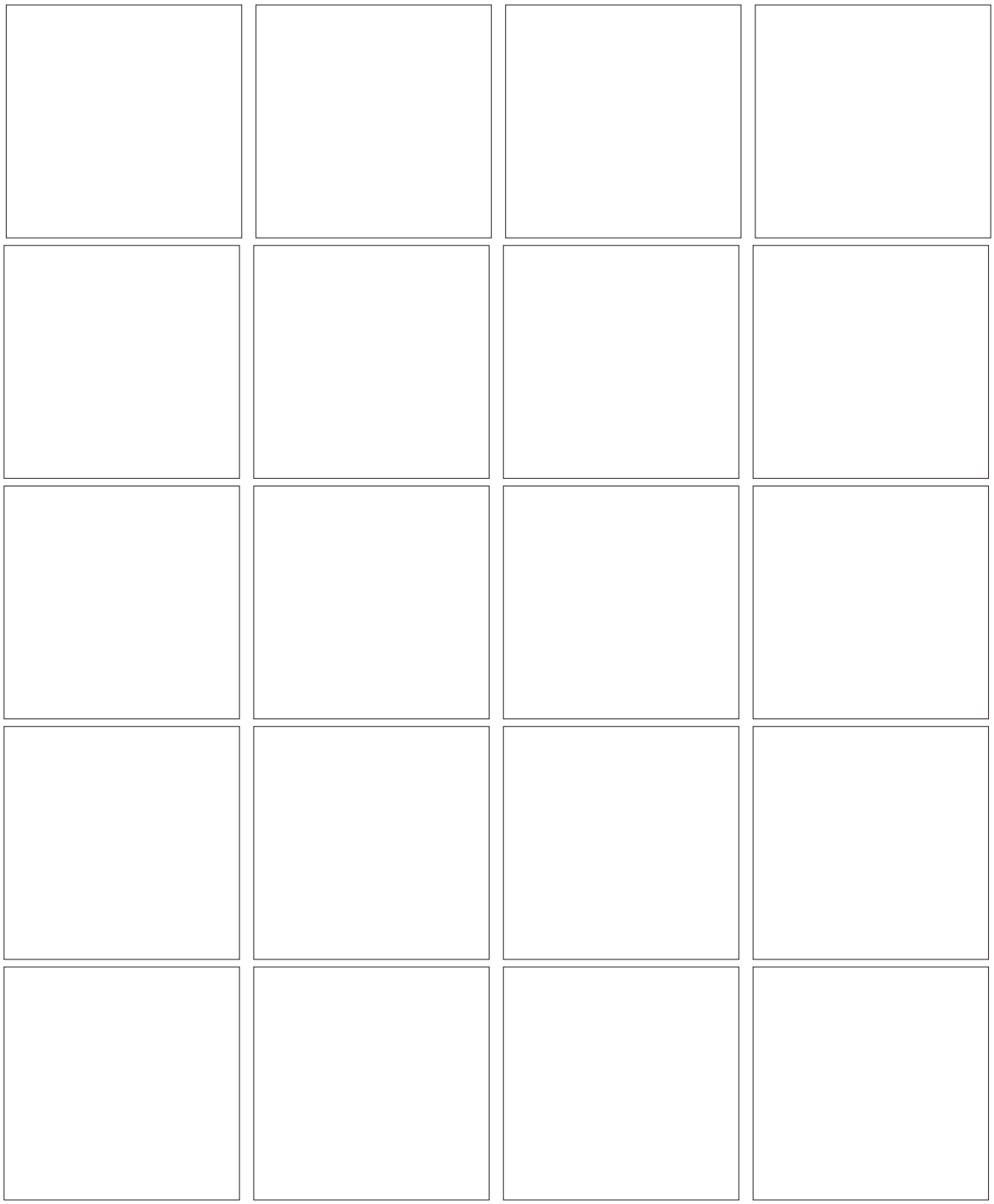

Figure B1. **(Insert here. 4 × 5 panels per figures × 4 figures?) The observed SEDs of the 63 strong LAEs in the COSMOS field with their thumbnails in broad- and intermediate-bands. The observed data points are shown by filled circles with error bars. Among them, the broadbands whose wavelength coverage overlaps with the excess IA band are represented by the grey symbols separately because these broadbands are not used in the SED fitting to determine the best-fit model SED shown by the blue solid curve.**